



Contents lists available at ScienceDirect

## Journal of Sound and Vibration

journal homepage: [www.elsevier.com/locate/jsvi](http://www.elsevier.com/locate/jsvi)

# Origins of broadband vibration attenuation empowered by optimized viscoelastic metamaterial inclusions



Sih-Ling Yeh, Ryan L. Harne\*

Department of Mechanical and Aerospace Engineering, The Ohio State University, Columbus, OH, 43210, USA

## ARTICLE INFO

## Article history:

Received 12 February 2019

Received in revised form 10 June 2019

Accepted 12 June 2019

Available online 14 June 2019

## ABSTRACT

Many engineering applications involve slender tubular structures subjected to potentially harmful vibrations that must be damped to sustain the working life of the system. This research takes recent experimental observations involving cylindrical metamaterials, ideal for such tubular structures, and uncovers the precise working mechanisms that trigger broadband vibration damping when embedded into cylindrical structural systems. An analytical model of the viscoelastic inclusions is first enhanced, drawing in part from recent studies. Then a new optimization approach is established based on a genetic algorithm. Following verification by finite element simulations and validation by experimental data, the optimized inclusions are scrutinized for the characteristics that culminate in exceptional damping of the host tube vibrations. The frequencies at which broadband vibration damping is achieved are found to coincide closely with the lowest order eigenfrequencies related to eigenmodes involving translational motion of the metamaterial core layer. The Young's modulus of annular and radially arrayed beam layers of the metamaterial is discovered to mostly influence frequency band where such modes occur, and a straightforward expression for the eigenfrequency relationships is uncovered. The design parameter relations and influences on the metamaterial response uncovered in this work help guide metamaterial formulations that maximize vibration attenuation of tubular structures.

© 2019 Elsevier Ltd. All rights reserved.

## 1. Introduction

Elastic metamaterials may exhibit negative refraction, wave propagation bandgaps, and local resonance characteristics that have significant implications for practices of vibration control and sensing [1]. This is because such properties cultivate unusual material behavior including extreme broadband wave attenuation, cloaking, wave guiding, and topological insulation. Geometric designs and material selections of the metamaterials are integral to realize such characteristics [2]. Due to the non-intuitive relations among geometry, material properties, and the resulting macroscopic material behaviors, researchers have employed parametric studies and optimization methods to uncover the metamaterial design methods that give rise to desired functionality.

Parametric studies often explore the influences of geometric parameters and material properties on the material behavior, such as how changes in Poisson's ratio, Young's modulus, and mass density may influence vibration mitigation. Peng et al. [3]

\* Corresponding author.

E-mail address: [harne.3@osu.edu](mailto:harne.3@osu.edu) (R.L. Harne).

and An et al. [4] report that tailoring the relative mass distributions in metamaterial plates with local resonances may increase the breadth of the stopband and enable lower frequency bandgaps. Essink and Inman [5] contrast how material selection may influence the balance among damping and vibration absorption mechanisms in engineered metastructures. Chen et al. [6] studies a lattice-based metamaterial that exhibits large variation of Poisson's ratio to tune the frequency range and number of bandgaps by change of compressive loading. For chiral metamaterials, the geometry of the embedded local resonators is central to the bandgap characteristics, as found through a variety of investigations [7–9].

Such parametric studies provide valuable knowledge on the relations between the desired material functionality and designed parameters. Yet, it is often a priority to reveal what characteristics of the metamaterial microstructure are most influential to govern the macroscopic behavior. To this end, optimization techniques are especially useful. For instance, Abdeljaber et al. [10] and Ranjbar et al. [11] use optimization approaches to shed light on the interactions between parametric design and vibration suppression in chiral metamaterials. Researchers have also optimized metamaterials for cloaking [12], mode conversion [13], bandgap maximization [14,15], energy dissipation through buckling [16], and tuned-mass-damper operation [17,18]. The studies exemplify that optimization may reveal the underlying mechanisms that are the primary source of the superior macroscopic material behavior.

Cylindrical metamaterials are previously found by the authors to give rise to exceptional shock mitigation when embedded in host structures [19]. The previous studies report on cylindrical-shaped, single material metamaterial inclusions embedded in a hollow cylindrical tube. For vibration environments, the inclusions also exhibit tuned mass damper (TMD) and constrained layer damping (CLD) behaviors for broadband vibration attenuation [20]. Yet, these prior observations do not uncover the underlying relationships among the design parameters, multi-material selections, and periodic metamaterial constituent combinations that cultivate exceptional broadband vibration attenuation. Consequently, there is a lack of understanding on how the cylindrical metamaterials manipulate and suppress broadband vibrations. Such knowledge gap limits the potential application of these metamaterials in many engineering environments.

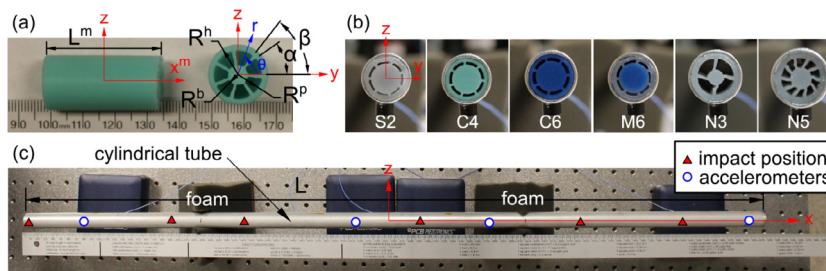
To fill the knowledge gap, this research develops an optimization technique to realize multi-material, elastomeric metamaterials that deliver broadband vibration attenuation in a host cylindrical tube, and examines the resulting optimized inclusion characteristics to understand the fundamental mechanisms that cultivate the macroscopic material behavior. First, the model formulation, including the deformations, energies, and the Euler-Lagrange governing equations are developed for the several viscoelastic material layers. The Euler-Lagrange equations are approximately solved by the Ritz method with trigonometric functions as the trial functions [21]. Then, the analytical method is supported by experimental validation and by numerical verification using finite element analysis. Next, the findings from three optimization studies are reported to broadly investigate the design selections that give rise to broadband vibration mitigation mechanisms. Finally, a summary is given of the key discoveries from this work and opportunities for future research.

## 2. Analytical model formulation

The analytical approach is established to explore how the metamaterial inclusions attenuate vibrations of the host structure. With this model framework, an optimization approach based on a genetic algorithm is formulated to identify the optimized metamaterial inclusions for specific performance objectives. Such optimized inclusion parameters are then scrutinized in Sec. 6 to uncover the working mechanisms for greatest broadband vibration attenuation. The analytical approach builds from the work by Yeh and Harne [20] in significant new ways, including expanding the study to multi-material inclusions, introduction of generalized viscoelastic material damping models, and consideration of new cross-section design parameters.

### 2.1. Overview of the host structure and metamaterial inclusions

The system in this study is a cylindrical hollow tube with metamaterial inclusions. The host structure is a hollow tube of length  $L$ , thickness  $T$ , and the inner radius  $R^h$ . The cylindrical tube is composed of a linear elastic material with Young's



**Fig. 1.** Photograph of (a) metamaterial inclusion, (b) metamaterial inclusions embedded in the cylindrical tube, and (c) experimental setup.

modulus  $E^h$ , density  $\rho^h$ , structural loss factor  $\eta^h$ , mass-proportional damping coefficient  $\alpha^h$ , and stiffness-proportional damping coefficient  $\beta^h$ . The superscript  $h$  indicates a host structure relevant parameter. The metamaterial inclusions are embedded into the cylindrical hollow tube at the right and left ends. Fig. 1(a) demonstrates the length  $L^m$  and cross-sectional geometry of the metamaterial inclusion, showing a central core surrounded by  $N$  radially arrayed beams, with a final outer annular layer at the periphery of the cross-section. The superscript  $m$  indicates a metamaterial relevant parameter:  $E^m$  is Young's modulus,  $\rho^m$  is density,  $\nu^m$  is Poisson's ratio,  $\eta^m$  is structural loss factor,  $\alpha^m$  is mass-proportional damping coefficient,  $\beta^m$  is stiffness-proportional damping coefficient, and  $C^m$  is Kelvin-Voigt damping coefficient.

To form the analytical model based on the exact geometry of the metamaterial inclusion, the cylindrical hollow tube with metamaterial inclusion is studied as a composite of four radial layers [20]. From the outermost radial layer to the innermost radial layer, the four layers are the host structure layer, the annular metamaterial layer, the porous metamaterial layer, and the core bulk metamaterial layer [20]. The superscripts  $b$ ,  $a$ , and  $p$  respectively refer to the bulk metamaterial, annular metamaterial, and porous metamaterial layers. As uniquely studied in this work, for multi-material inclusions each layer may utilize distinct materials. In the following notation, the superscript  $m$  is therefore replaced by  $b$ ,  $a$ , or  $p$  to refer to the unique material property for the respective layers. The materials used in this work are shown for the same geometry of single-material inclusions S2, C4, and C6 in Fig. 1(b), and respectively include elastomers with Shore 00-10, Shore 15 A, and Shore 30 A, as described in greater detail in Sec. 3. A multi-material inclusion M6 is also shown in Fig. 1(b), along with inclusions N3 and N5 that have 4 and 10 radially arrayed beams, respectively, extending from the central core. The cross-sectional geometries of the four layers in a cylindrical coordinate system  $(r, \theta, x^m)$  are listed in Table 1. In the model, the tube is excited by lateral harmonic point forces at the 201 random locations on the exterior cylindrical surface of the tube. Experimentally, the tube is excited by broadband lateral forces at locations shown in Fig. 1(c). Greater details on the experiments are provided in Sec. 3.

## 2.2. Displacements, kinetic energies, potential energies, energy dissipation, and work

The cylindrical hollow tube is long, slender, and undergoes small lateral displacements. As a result, Euler-Bernoulli beam theory is adopted to describe the lateral translation of the host structure in the host coordinate system  $(x, y, z)$ . Timoshenko beam theory is utilized to characterize the bending and shear deformations of the metamaterial inclusions in the metamaterial coordinate system  $(x^m, y, z)$  because the inclusions are short and non-slender. Furthermore, when embedded into the tube, the metamaterial inclusions are slightly compressed. The porous metamaterial and bulk metamaterial layers consider torsional deformations because the slight compression may lead the radially arrayed beams rotate around the  $x$  axis, as shown for inclusions N3 and N5 embedded in the cylindrical tube in Fig. 1(b). The annular metamaterial shear angles  $\psi^a$ , porous metamaterial shear angles  $\psi^p$ , and torsional angles  $\alpha^p$  are linearly distributed along the radial  $r$  coordinate from the host structure to the bulk metamaterial. Table 1 lists the displacements of the host structure  $\mathbf{u}^h$ , bulk metamaterial  $\mathbf{u}^b$ , porous metamaterial  $\mathbf{u}^p$ , and annular metamaterial  $\mathbf{u}^a$  layers, defined in terms of the four degrees-of-freedom (DOFs) of the system. These distinct DOFs include the host structure transverse displacement  $w^h = w^h(x, t)$ , the bulk metamaterial lateral displacement  $w^b = w^b(x^m, t)$ , shear angle  $\psi^b = \psi^b(x^m, t)$  in the  $x^m z$  plane, and torsional angle  $\alpha^b = \alpha^b(x^m, t)$  in the  $yz$  plane.

The kinetic Eq. (3) and potential Eq. (4) energies are determined by evaluating velocities and strains for each layer.

**Table 1**

Geometries and displacements of the host, bulk metamaterial, annular metamaterial, porous metamaterial layers.

layer	geometry	displacement
host	$R^h < r < R_0^h$ ; $0 < \theta < 2\pi$ ; $-L/2 < x < L/2$	$u_x^h = -zw_x^h$ ; $u_y^h = 0$ ; $u_z^h = w^h$
bulk	$0 < r < R^b$ ; $0 < \theta < 2\pi$ ; $-L^m/2 < x^m < L^m/2$ ; $m = 1, 2$	$u_x^b = -z\psi^b$ ; $u_y^b = -z\alpha^b$ ; $u_z^b = w^b + y\alpha^b$
annular	$R^p < r < R^h$ ; $0 < \theta < 2\pi$ ; $-L^m/2 < x^m < L^m/2$ ; $m = 1, 2$	$u_x^a = -z\psi^a = -z\left(\frac{r-R^b}{R^h-R^b}w_x^h + \frac{R^h-r}{R^h-R^b}\psi^b\right)$ ; $u_y^a = 0$ ; $u_z^a = w^a = \frac{r-R^b}{R^h-R^b}w^h + \frac{R^h-r}{R^h-R^b}w^b$
porous	$R^b < r < R^p$ ; $\theta_{1n} < \theta < \theta_{2n}$ ; $\theta_{1n} = \alpha + (n-1)\beta$ ; $\theta_{2n} = n\beta$ ; $n = 1, 2, \dots, N^a$ ; $-L^m/2 < x^m < L^m/2$ ; $m = 1, 2$	$u_x^p = -z\psi^p = -z\left(\frac{r-R^b}{R^h-R^b}w_x^h + \frac{R^h-r}{R^h-R^b}\psi^b\right)$ ; $u_y^p = -z\alpha^p = -z\frac{R^h-r}{R^h-R^b}\alpha^b$ ; $u_z^p = w^p + y\alpha^p = \frac{r-R^b}{R^h-R^b}w^h + \frac{R^h-r}{R^h-R^b}w^b + y\frac{R^h-r}{R^h-R^b}\alpha^b$

<sup>a</sup>  $N$  is the number of radially arrayed beams.

$$T = \frac{1}{2} \int_{-L/2}^{L/2} \int_{R^h}^{R_o^h} \int_0^{2\pi} \rho^h (\mathbf{u}_t^h)^T \mathbf{u}_t^h r dr d\theta dx$$

$$+ \frac{1}{2} \sum_{m=1}^2 \int_{-L^m/2}^{L^m/2} \left\{ \int_0^{2\pi} \left[ \int_0^{R^b} \rho^b (\mathbf{u}_t^b)^T \mathbf{u}_t^b r dr + \int_{R^p}^{R^h} \rho^a (\mathbf{u}_t^a)^T \mathbf{u}_t^a r dr \right] d\theta \right. \\ \left. + \sum_{n=1}^N \int_{\theta_{1n}}^{\theta_{2n}} \int_{R^b}^{R^p} \rho^p (\mathbf{u}_t^p)^T \mathbf{u}_t^p r dr d\theta \right\} dx^m \tag{3}$$

$$U = \frac{1}{2} \int_{-L/2}^{L/2} \int_{R^h}^{R_o^h} \int_0^{2\pi} \tilde{E}^h (\boldsymbol{\varepsilon}^h)^T \boldsymbol{\varepsilon}^h r dr d\theta dx$$

$$+ \frac{1}{2} \sum_{m=1}^2 \int_{-L^m/2}^{L^m/2} \left\{ \int_0^{2\pi} \left\{ \int_0^{R^b} \left[ \tilde{E}^b (\boldsymbol{\varepsilon}^b)^T \boldsymbol{\varepsilon}^b + \tilde{G}^b k^b (\boldsymbol{\gamma}^b)^T \boldsymbol{\gamma}^b \right] r dr \right\} d\theta \right. \\ \left. + \int_{R^p}^{R^h} \left[ \tilde{E}^a (\boldsymbol{\varepsilon}^a)^T \boldsymbol{\varepsilon}^a + \tilde{G}^a k^a (\boldsymbol{\gamma}^a)^T \boldsymbol{\gamma}^a \right] r dr \right\} dx^m \\ \left. + \sum_{n=1}^N \int_{\theta_{1n}}^{\theta_{2n}} \int_{R^b}^{R^p} \left[ \tilde{E}^p (\boldsymbol{\varepsilon}^p)^T \boldsymbol{\varepsilon}^p + \tilde{G}^p k^p (\boldsymbol{\gamma}^p)^T \boldsymbol{\gamma}^p \right] r dr d\theta \right\} dx^m \tag{4}$$

Here,  $\tilde{E}^h = E^h(1 + j\eta^h)$ ,  $\tilde{E}^b = E^b(1 + j\eta^b)$ ,  $\tilde{E}^p = E^p(1 + j\eta^p)$ , and  $\tilde{E}^a = E^a(1 + j\eta^a)$  are the complex Young’s modulus of the host tube and of the bulk, porous, and annular metamaterial layers, respectively. The  $\tilde{G}^b = \tilde{E}^b/[2(1 + \nu^b)]$ ,  $\tilde{G}^p = \tilde{E}^p/[2(1 + \nu^p)]$ , and  $\tilde{G}^a = \tilde{E}^a/[2(1 + \nu^a)]$  are the complex shear modulus of the bulk, porous, and annular metamaterial layers, respectively. The shear coefficients for the annular metamaterial layer  $k^a = 2(1 + \nu^a)/(4 + 3\nu^a)$ , porous metamaterial layer  $k^p = 10(1 + \nu^p)/(12 + 11\nu^p)$ , and the bulk metamaterial layer  $k^b = 6(1 + \nu^b)/(7 + 6\nu^b)$  are derived by Cowper [22] based on the cross-section geometries of each layer.

To characterize the energy dissipation in the viscoelastic metamaterial inclusions, this study newly includes Kelvin-Voigt viscoelastic damping. Based on the concept of the dissipation function for a Timoshenko beam [23–26], the Rayleigh dissipation function of the metamaterial inclusion  $R$  is

$$R = \frac{1}{2} \sum_{m=1}^2 \int_{-L^m/2}^{L^m/2} \left\{ \int_0^{2\pi} \left\{ \int_0^{R^b} C^b \left[ (\boldsymbol{\varepsilon}_t^b)^T \boldsymbol{\varepsilon}_t^b + (\boldsymbol{\gamma}_t^b)^T \boldsymbol{\gamma}_t^b \right] r dr \right\} d\theta \right. \\ \left. + \int_{R^p}^{R^h} C^a \left[ (\boldsymbol{\varepsilon}_t^a)^T \boldsymbol{\varepsilon}_t^a + (\boldsymbol{\gamma}_t^a)^T \boldsymbol{\gamma}_t^a \right] r dr \right\} dx^m \\ \left. + \sum_{n=1}^N \int_{\theta_{1n}}^{\theta_{2n}} \int_{R^b}^{R^p} C^p \left[ (\boldsymbol{\varepsilon}_t^p)^T \boldsymbol{\varepsilon}_t^p + (\boldsymbol{\gamma}_t^p)^T \boldsymbol{\gamma}_t^p \right] r dr d\theta \right\} dx^m \tag{5}$$

The  $C^b$ ,  $C^a$ , and  $C^p$  are the Kelvin-Voigt damping coefficient of bulk metamaterial, annular metamaterial, and porous metamaterial layers, respectively.

The work  $W$  of the applied lateral force per unit length  $f(x, t)$  on the host tube in the  $x$  coordinate is

$$W = \int_{-L/2}^{L/2} w^h f(x, t) dx \tag{6}$$

### 2.3. Euler-Lagrange governing equations and Ritz method

The Ritz method is employed to reduce the system dependence to only time and to obtain the Euler-Lagrange governing equations for the system. To apply the trigonometric trial functions by the Ritz method [21], the axial coordinates of the host tube  $x$  and each metamaterial inclusion  $x^m$  are normalized using

$$\xi = \frac{2x}{L}, \xi^m = \frac{2x^m}{L^m} \quad (7a-b)$$

The relationship between the normalized coordinate of the host  $\xi$  and each metamaterial  $\xi^m$  is

$$\xi = \xi_m + \frac{L^m}{L} \xi^m \quad (8)$$

where the  $\xi_m$  is the center of the metamaterial inclusion in the  $\xi$  coordinate.

A set of trigonometric functions  $\phi_k(\eta)$  created by Beslin and Nicolas [21] is adopted as the trial functions in the Ritz method expansion [27]. The trigonometric functions  $\phi_k(\eta)$  used as the trial functions are

$$\phi_k(\eta) = \sin(a_k\eta + b_k)\sin(c_k\eta + d_k) \quad (9)$$

The coefficients  $a_k$ ,  $b_k$ ,  $c_k$ , and  $d_k$  are listed in Ref. [21]. The host lateral displacement  $w^h$ , core bulk metamaterial lateral displacement  $w^b$ , shear angle  $\psi^b$ , and torsional angle  $\alpha^b$  are

$$\begin{aligned} w^h(\xi, t) &= a_f^{hb}(t)\phi_f^{hb}(\xi) \\ w^b(\xi^m, t) &= b_g^{mb}(t)\phi_g^{mb}(\xi^m) \\ \psi^b(\xi^m, t) &= c_h^{ms}(t)\phi_h^{ms}(\xi^m) \\ \alpha^b(\xi^m, t) &= d_i^{mt}(t)\phi_i^{mt}(\xi^m) \end{aligned} \quad (10a-d)$$

The  $a_f^{hb}$ ,  $b_g^{mb}$ ,  $c_h^{ms}$ , and  $d_i^{mt}$  are unknown generalized coordinates to be determined, and  $\phi_f^{hb}$ ,  $\phi_g^{mb}$ ,  $\phi_h^{ms}$ , and  $\phi_i^{mt}$  are trial functions defined according to Eq. (9), where  $\eta$  is replaced by  $\xi$  or  $\xi^m$ , and  $k$  is replaced by  $f$ ,  $g$ ,  $h$ , or  $i$ . The superscripts  $hb$ ,  $mb$ ,  $ms$ , and  $mt$  refer to host lateral displacement, metamaterial lateral displacement, metamaterial shear angle, metamaterial torsional displacement, respectively. In this study, 20, 10, 8, and 8 trial functions are adopted in the Ritz expansion of the host structure lateral displacement, metamaterial lateral displacement, shear angle, and torsional angle, respectively.

The Euler-Lagrange governing equations for the system are

$$\frac{d}{dt} \left( \frac{\partial L}{\partial \dot{a}_f^{hb}} \right) - \frac{\partial L}{\partial a_f^{hb}} + \frac{\partial R}{\partial a_f^{hb}} = 0 \quad (11a)$$

$$\frac{d}{dt} \left( \frac{\partial L}{\partial \dot{b}_g^{mb}} \right) - \frac{\partial L}{\partial b_g^{mb}} + \frac{\partial R}{\partial b_g^{mb}} = 0 \quad (11b)$$

$$\frac{d}{dt} \left( \frac{\partial L}{\partial \dot{c}_h^{ms}} \right) - \frac{\partial L}{\partial c_h^{ms}} + \frac{\partial R}{\partial c_h^{ms}} = 0 \quad (11c)$$

$$\frac{d}{dt} \left( \frac{\partial L}{\partial \dot{d}_i^{mt}} \right) - \frac{\partial L}{\partial d_i^{mt}} + \frac{\partial R}{\partial d_i^{mt}} = 0 \quad (11d)$$

where the Lagrangian of the coupled system is  $L = T - U + W$ . The governing equations are assumed to be steady-state time-harmonic responses. As a result, the unknown generalized coordinates and the lateral force applied on the host structure exhibit time dependence of the form

$$a_f^{hb} = A_f^{hb} e^{j\omega t}, b_g^{mb} = B_g^{mb} e^{j\omega t}, c_h^{ms} = C_h^{ms} e^{j\omega t}, d_i^{mt} = D_i^{mt} e^{j\omega t}, f = F_f^{hb} e^{j\omega t} \quad (12a-e)$$

Substituting Eq. (12) into Eq. (11), the governing equations in matrix form are

$$\left( -\omega^2 \mathbf{M} + j\omega \mathbf{C} + \mathbf{K} \right) \mathbf{q} = \mathbf{F} \quad (13)$$

$$\mathbf{q} = \left\{ A_f^{hb} \quad B_g^{1b} \quad C_h^{1s} \quad D_i^{1t} \quad \dots \quad B_g^{mb} \quad C_h^{ms} \quad D_i^{mt} \right\}^T \quad (14)$$

$$\mathbf{F} = \left\{ \frac{L}{2} \int_{-1}^1 F \phi_f^{hb} d\xi \quad 0 \quad 0 \quad 0 \quad \dots \quad 0 \quad 0 \quad 0 \right\}^T \quad (15)$$

The damping matrix  $\mathbf{C}$  is composed of Rayleigh damping matrix  $\mathbf{C}^R$  and the Kelvin-Voigt damping matrix  $\mathbf{C}^{KV}$ , so that  $\mathbf{C} = \mathbf{C}^R + \mathbf{C}^{KV}$ . The Rayleigh damping coefficients of host structure and metamaterial are distinct so Rayleigh damping matrix is  $\mathbf{C}^R = \alpha^m \text{Re}[\mathbf{M}] + \beta^m \text{Re}[\mathbf{K}]$ , whereas the element of the host tube in Rayleigh damping matrix is  $(C_{fp}^{hbhb})^R = \alpha^h \text{Re}[M_{fp}^{hbhb}] + \beta^h \text{Re}[K_{fp}^{hbhb}]$ . The unknown constants  $\mathbf{q}$  and forcing vector  $\mathbf{F}$  are respectively Eq. (14) and Eq. (15). The detailed components of the mass matrix  $\mathbf{M}$ , stiffness matrix  $\mathbf{K}$ , and Kelvin-Voigt damping matrix  $\mathbf{C}^{KV}$  are listed in Appendix A.1, A.2, and A.3, respectively.

Solutions for the unknown constants  $\mathbf{q}$  are calculated by Gaussian elimination applied to Eq. (13). Then, substituting the unknown constants into Eq. (14) and trial functions Eq. (9) into Eq. (10), the lateral translation of the host, metamaterial lateral translations, metamaterial shear angles, and metamaterial torsional angles of the inclusions are subsequently obtained.

### 3. Experimental setup

The experimental system consists of a freely suspended cylindrical aluminum tube that may have a metamaterial inclusion placed at each end of the tube. Triangular foam wedges are used to approximate the free-free boundary condition, as shown in Fig. 1(c). The two metamaterial inclusions are embedded at the ends of the tube. The tube and inclusions terminate at the same cross-section, as shown in Fig. 1(b). For each experiment that involves the metamaterial inclusions, the two inclusions that are used at the tube ends have the same nominal metamaterial dimensions and material selections. In order to secure the inclusions inside the host tube, the outer radius of the inclusion is 1% greater than the inner radius of the host tube. The geometric parameters of the tube and inclusions are listed in Table 2. The metamaterial inclusions are made from silicone rubber. Fig. 1(b) shows inclusions fabricated using each of the three silicone rubbers (Smooth-on, Inc.) considered in this work. In increasing bulk modulus, the silicone rubbers are Ecoflex 00-10 (EF10, Shore hardness 00-10), Mold Star 15S (MS15, Shore hardness 15A), and Mold Star 30 (MS30, Shore hardness 30A). In Fig. 1(c), the filled triangle markers and unfilled circular markers represent the impact positions and accelerometers, respectively. The experiments are conducted by impacting the host tube at six locations using a modal hammer (PCB 086C01) and then by measuring acceleration (PCB 352A24) at four locations. These transient signals are recorded and used to determine the frequency response of the host tube with and without the inclusions. Each experimental frequency response is an average of the individual results from 30 hits at each of the six impact locations. Using the data, the relevant metric of comparison is the transfer function between the output global acceleration and the input force.

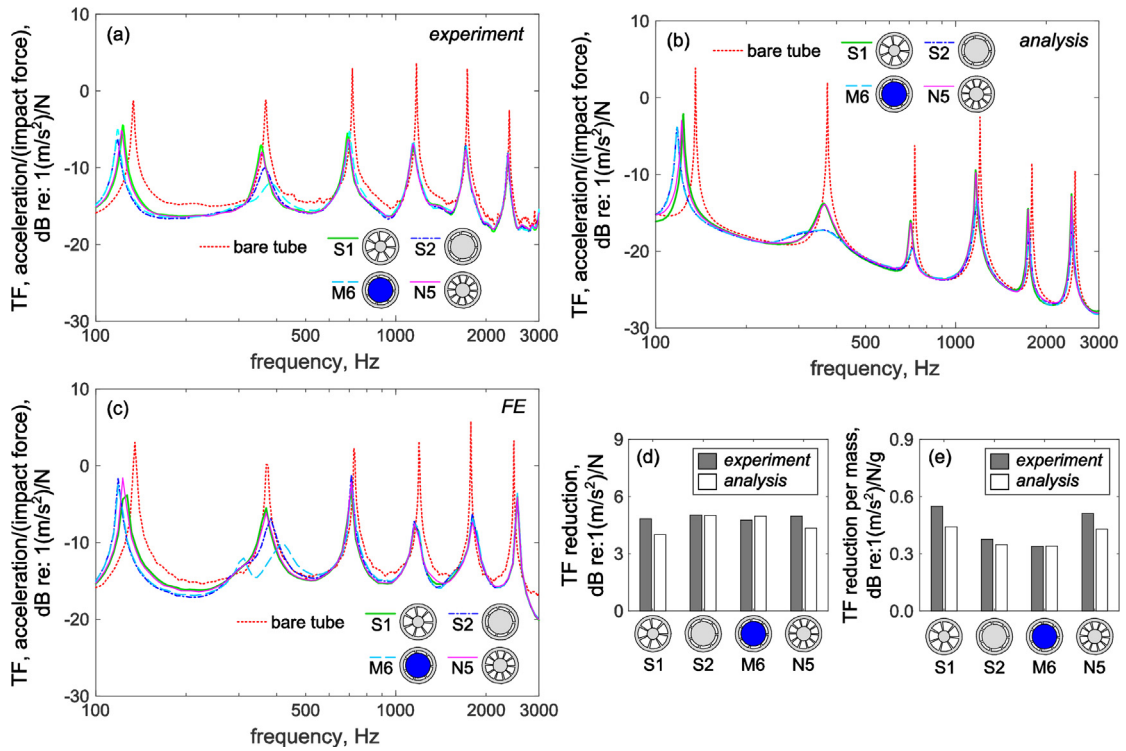
### 4. Experimental validation and numerical verification

Prior to investigating optimal methods of design and implementation of the metamaterial inclusion, the analytical model is validated by experiments and verified against finite element (FE) modeling.

Fig. 2 presents results from the frequency response transfer functions (TFs) of the bare cylindrical tube and the tube with pairs of metamaterial inclusions placed at both tube ends. Fig. 2(a) shows experimental data and Fig. 2(b) shows the analytical result. The insets of these figures feature the cross-section geometry of the inclusions, whose colors represent the different silicone rubbers employed: in the insets, grey refers to EF10, cyan refers to MS15, and blue refers to MS30. In Fig. 2, the four metamaterial inclusions include S1, S2, M6, and N5, and the corresponding cross-section parameters are listed in Table 4.

**Table 2**  
Geometric parameters of the cylindrical hollow tube and the metamaterial inclusions.

item	unit	value
tube length, $L$	m	0.91
tube inner radius, $R^h$	mm	8.28
tube thickness, $T$	mm	1.25
inclusion length, $L^m$	mm	34.94
inclusion outer radius	mm	8.36
annular layer thickness, $R^h - R^p$	mm	1.5



**Fig. 2.** Comparisons of four metamaterial inclusions, including S1, S2, M6, and N5. (a) Experimental TF frequency responses, (b) analytical TF frequency responses, (c) finite element (FE) model frequency responses, (d) experimental and analytical TF reductions, and (e) experimental and analytical TF reductions per mass from 85 Hz to 2850 Hz.

Inclusion S1, shown in Fig. 1(b), is fabricated using EF10 and has 7 radially arrayed beams with radius ratio  $R^b/R^h = 0.32$  and open angle ratio  $\alpha/\beta = 0.85$ . The inclusion S2 is also made using EF10 and has 7 radially arrayed beams, yet uses the radius ratio  $R^b/R^h = 0.68$  and open angle ratio  $\alpha/\beta = 0.87$ . For inclusion M6, shown in Fig. 1(b), the porous and annular metamaterial layers are made with EF10 while the core bulk metamaterial layer is made with MS30. Experimentally, this multi-material molding is achieved in two molding stages since the pre-cured silicone rubber will cure and bond with post-cured silicone rubber pieces. The radius ratio of inclusion M6 is  $R^b/R^h = 0.69$  and open angle is  $\alpha/\beta = 0.87$ . Inclusion N5, shown in Fig. 1(b), is made with EF10 using 10 radially arrayed beams having radius ratio  $R^b/R^h = 0.40$  and open angle ratio  $\alpha/\beta = 0.83$ . Damping constants for the structural loss factor, proportional, and Kelvin-Voigt damping models are also given in Table 3. These constants are determined through model curve fitting to empirical trends. Proportional damping is warranted on the basis of neglecting rigid body motion for the freely supported host tube structure [28].

Comparing Fig. 2(a) and (b), the first mode of the cylindrical tube is around 120 Hz. The frequency shifts around the first mode caused by the introduction of the inclusions are in good agreement between analysis and experiments. For the second mode of the tube around 360 Hz, the vibration attenuation provided by inclusion N5 is slightly less than that provided by inclusion S1, which is observed in the analytical and experimental results. In addition, the vibration attenuation achieved around the second mode is approximately the same whether inclusions S2 or M6 are employed, whereas experimentally inclusion M6 provides slightly greater vibration attenuation than inclusion S2. For the higher frequency resonances of the tube, it is difficult to compare narrowband characteristics of the TFs so that the overall TF reductions are useful for a quantitative contrast. Fig. 2(d) and (e) present the TF reductions and TF reductions per mass from 85 to 2850 Hz for the four inclusions. Although there are minor discrepancies between experiment and analysis shown in Fig. 2(a) and (b), the overall similarity between experimental and analytical results in these important broadband vibration metrics shown in Fig. 2(d) and (e) provides key validation to the analytical formulation.

A three-dimensional, solid FE model (COMSOL Multiphysics, Stockholm, Sweden) is created to simulate the forced vibration responses of the cylindrical tube with and without metamaterial inclusions. The FE model geometry is composed using the complete system characteristics described in the analytical formulation, Sec. 2. The impact force is applied at  $(x, y, z) = (-L/2 + L^m, 0, R^h + T)$  in the host structure coordinate system. In the analytical model, the displacements in porous and annular metamaterial layers are assumed to be linearly distributed along the  $r$  coordinate. Such assumption constrains the deformation of the metamaterial inclusion and increases the macroscopic stiffness. In order to compensate for such stiffening effect induced by the assumptions in analysis, the Young's moduli in the FE model are approximately 2.5 times greater than

**Table 3**  
Material properties of the cylindrical hollow tube and metamaterial inclusions.

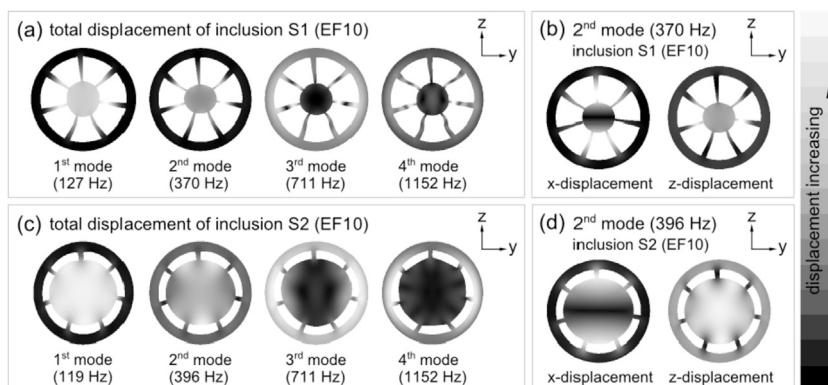
	tube	EF10		MS15		MS30	
		analysis	FE	analysis	FE	analysis	FE
Young's modulus, kPa	$68.9 \times 10^6$	60	200	300	800	600	1200
Poisson's ratio	0.33	0.49	0.49	0.49	0.49	0.49	0.49
density, kg/m <sup>3</sup>	2700	1145	1145	1145	1145	1145	1145
structural loss factor	0.002	0.02	0.2	0.02	0.2	0.02	0.2
mass-proportional damping	$1 \times 10^{-9}$	$2 \times 10^{-5}$	–	$2 \times 10^{-5}$	–	$2 \times 10^{-5}$	–
stiffness-proportional damping	$1 \times 10^{-9}$	$4 \times 10^{-5}$	–	$4 \times 10^{-5}$	–	$4 \times 10^{-5}$	–
Kelvin-Voigt damping	–	10	–	10	–	10	–

those moduli in the analytical model. The FE model also only permits use of structural damping in the metamaterial inclusions. As such, since the analytical comparison to data discovered multiple damping mechanisms contribute to the overall damping behavior of the metamaterial inclusions, the FE model uses structural loss factors that are 10 times greater than those in the analysis. Since both the FE model and analytical formulation are curve fit to the amplitudes of the experimentally measured resonances before and after introduction of the metamaterial inclusions, the relative constraining effect of the analytical assumptions and use of fewer damping models in the FE simulations enables both theoretical and computational tools to be compared against experimental data.

The frequency response of the cylindrical tube with and without four different metamaterial inclusions as computed from the FE model is shown in Fig. 2(c). Except for the notch at 345 Hz around the second mode of the cylindrical tube with inclusion M6, the FE results strongly agree with the experiments. On the other hand, the FE model requires almost five orders of magnitude longer time to compute than analysis. As a result, the analytical approach is utilized to arrive at insight by an optimization of the metamaterial inclusions for broadband vibration attenuation, whereas the FE method is used to complement discoveries by scrutinizing the detailed vibration attenuation mechanisms.

The total displacements of the inclusions S1 and S2 made with the most compliant material EF10 are shown in Fig. 3(a) and (c) as generated by the FE model. The total displacement is the square root of the sum of squares of the amplitudes of displacement components in  $x$ -,  $y$ -, and  $z$ - directions. For the first and second modes of the tube (S1: 127 Hz and 370 Hz; S2: 119 Hz and 396 Hz), the greatest deformations are centralized in the bulk metamaterial layers. Considering the radially arrayed beams to be analogous with springs, and considering the bulk core layer to be analogous with a lumped mass, that suggests that the coupled system is comparable to a tuned mass damper (TMD). For the third and fourth modes of the tube (S1: 711 Hz and 1152 Hz; S2: 711 Hz and 1152 Hz), the bulk metamaterial layers are less deformed when compared to the local deformations in porous and annular metamaterial layers. Based on such distribution of local deformation, the metamaterial inclusion acts in a way similar to constrained layer damping (CLD). These new findings explicitly support the technical hypotheses made in prior work on the cylindrical inclusion geometries [20].

To examine the dynamic behavior of the TMD vibration attenuation mechanism at the second mode in further detail, Fig. 3(b) and (d) present the  $x$  and  $z$  displacement amplitude contours for inclusions S1 and S2. For these cases, the bulk metamaterial layers are seen to displace both vertically and laterally to vibrate. In other words, the metamaterial inclusion deforms in a way like a translational-and-shear-based TMD instead of a pure translational TMD. It may be concluded that the



**Fig. 3.** Displacement contours of cross-sections for inclusions S1 and S2. (a) Total displacement contours of inclusion S1 for the lowest four modes, (b)  $x$ - and  $z$ -displacement contours of inclusion S1 at the second mode, (c) total displacement contours of inclusion S2 for the lowest four modes, and (d)  $x$ - and  $z$ -displacement contours of inclusion S2 at the second mode.



greater vibration attenuation around the second mode, than the first mode, is due to such combined translational-and-shear TMD behavior. The dynamic characteristics of translational-and-shear TMD are fully assessed in Sec. 6.5.

## 5. Genetic algorithm optimization approach

The authors' prior work suggested that the dynamic stiffness strongly governs the ability for the metamaterial inclusions to attenuate broadband vibration [20]. The prior work suggested that the dynamic stiffness was modified by change in the radius ratio  $R^b/R^h$ , open angle ratio  $\alpha/\beta$ , number of radially arrayed beams in the porous metamaterial  $N$ , and Young's modulus of inclusion. Therefore, this study considers these parameters as key variables to change to achieve optimal broadband vibration attenuation and help to uncover the working mechanisms that cultivate such dynamic behavior.

This study leverages a genetic algorithm (GA) to illuminate optimized inclusion geometries that give rise to the greatest vibration attenuation. In the GA-based optimization approach, an initial population of 100 individuals is seeded using randomly generated design parameters around nominal values. There are two objective functions, A and B, used in this study. Objective function A is the total attenuation of tube vibration, whereas objective function B is the total vibration attenuation per inclusion mass. The vibration attenuation is the square root of the sum of squares of the TFs from 85 to 2850 Hz. After computing the objective functions for each individual in the population and ranking the individuals, the 50 highest-ranked individuals are kept without change in the next new generation. This provides a 50% selection rate from one generation to the next. These 25 pairs of selected "parents" perform random mating using single-point parametric crossover, and have two "children" per pair. Therefore, the remaining 50 individuals of the new generation are offspring resulting from the 50 highest-ranked individuals. Then, given this new generation of 100 individuals, 20 of the individuals experience random mutation of parameters, providing a 20% mutation rate. In this research, sufficiently before 100 generations of this evolutionary sequence are evaluated and evolved, the design parameters of inclusions are seen to converge. As a result, the convergence criterion to stop the GA evaluation is set to be 100 generations.

## 6. Results and discussions

Yeh and Harne [20] found evidence that the primary characteristic tailored by change in the radius ratio and open angle ratio is the dynamic stiffness of the inclusion. It was also observed that change in damping of the inclusion material mostly influenced the magnitudes of the resulting system resonances yet did not otherwise substantially tailor the resonant frequencies [20]. In addition to these two parameters of radius ratio and open angle ratio, it is also intuitive that the dynamic stiffness may be modified by change in the Young's modulus of the inclusion and by the number of radially arrayed beams. In order to determine the most influential inclusion design parameters that deliver the maximum broadband vibration, here the optimization approach described in Sec. 5 is leveraged. Then, by scrutinizing the optimal inclusion designs, the origins of the dynamic behavior that give rise to the exceptional vibration attenuation are uncovered through detailed study of the optimized inclusion characteristics.














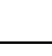
### 6.1. Optimization for single-material metamaterial inclusions

To optimize the metamaterial inclusions composed from a single material, the radius ratio, open angle ratio, and the Young's modulus are the parameters of interest. The number of radially arrayed beams in the porous metamaterial layer is 7 throughout the following optimization. For objective function B that maximizes total vibration attenuation per inclusion mass, the optimized design is inclusion S1, which is an inclusion composed from the silicone rubber EF10 having radius ratio  $R^b/R^h = 0.32$  and open angle ratio  $\alpha/\beta = 0.85$ . The optimized inclusion identified by the GA with objective function A that maximizes total attenuation is inclusion S2, which is composed from EF10 having radius ratio  $R^b/R^h = 0.68$  and open angle ratio  $\alpha/\beta = 0.87$ . The cross-section geometries of inclusions S1 and S2 are shown in Table 4.

Fig. 4(a) and (b) are respectively experimental and analytical frequency responses of tube vibration when inclusions S1, S2, C3, C4, C5, and C6 are applied at each tube end. The labeling technique for the inclusions considered here uses "S" to refer that the inclusion geometry is optimized for the case of a single-material inclusion. Odd and even numbers, respectively, indicate that the inclusions are determined by optimizations using either objective function B or objective function A. The inclusions labeled with "C" are comparison inclusions and are not optimized but provide a contrast to the optimized design parameters. The cross-section geometries of inclusions C3 and C5 are identical to S1, but employ the MS15 and MS30 materials, respectively, instead of the EF10 used for S1. Likewise, inclusions C4 and C6 are identical to inclusion S2 in design excepting the material, since C4 and C6 use MS15 and MS30 materials, respectively, whereas S2 uses EF10. The detailed parameters of the six inclusions are listed in Table 4.

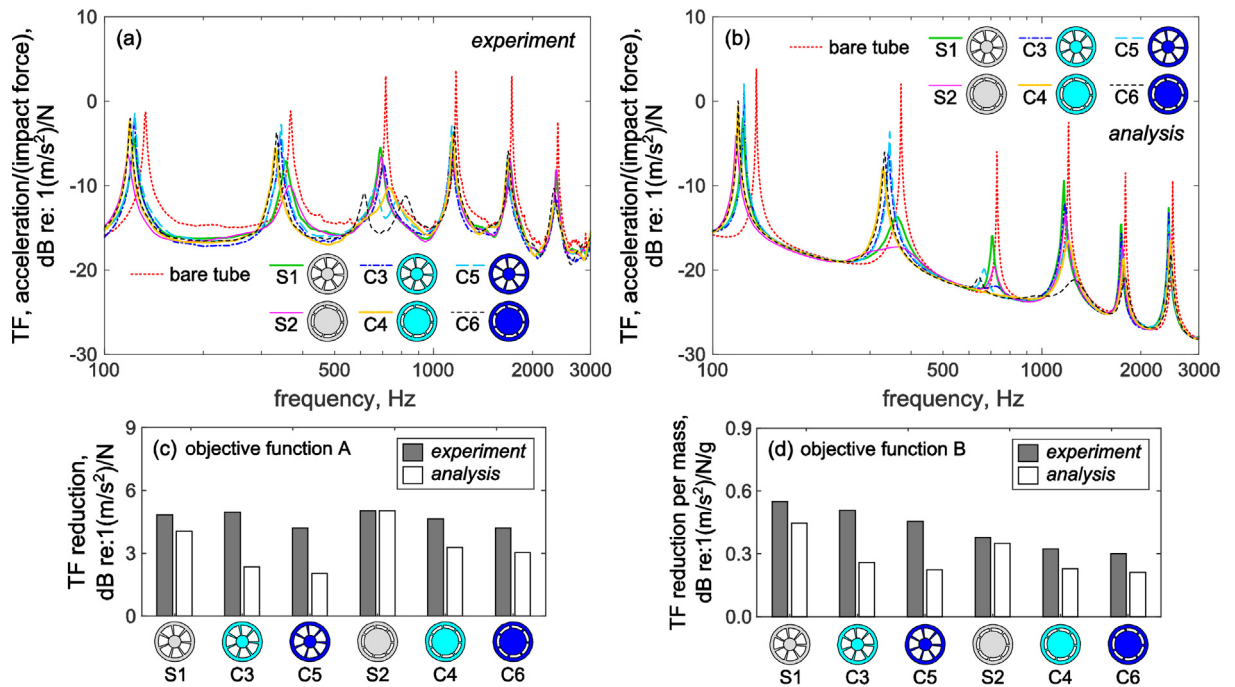
For the EF10 inclusions S1 and S2, when inserted into the host tube, both inclusions lead to greater broadband vibration attenuation than the other inclusions at frequencies higher than the second resonance, as seen in Fig. 4(a and b). This trend is observed in experiment and analysis. Here, this behavior is termed the "starting mode" for the more substantial vibration attenuation. For the MS15 and MS30 inclusions, which are C3, C4, C5, and C6, the more substantial vibration attenuation occurs after the third modes in Fig. 4(a and b). This means that for C4, C4, C5, and C6, the "starting mode" is the third mode. It is also observed in Fig. 4(a and b) that the frequency around the starting mode for the greater broadband vibration attenuation

**Table 4**  
Geometric parameters, materials, and eigenfrequencies of inclusions.

inclusion		bulk	porous & annular	$R^b/R^h$	$\alpha/\beta$	$N$	natural frequencies, Hz					
							1st	2nd	3rd	4th	5th	6th
S1		EF10	EF10	0.32	0.85	7	<u>218</u>	<u>346</u>	363	373	382	410
S2		EF10	EF10	0.68	0.87	7	<u>183</u>	345	<u>357</u>	360	380	408
C3		MS15	MS15	0.32	0.85	7	<u>438</u>	<u>693</u>	728	753	768	836
C4		MS15	MS15	0.68	0.87	7	<u>367</u>	690	<u>714</u>	720	760	815
C5		MS30	MS30	0.32	0.85	7	<u>535</u>	<u>846</u>	888	915	935	1005
C6		MS30	MS30	0.68	0.87	7	<u>449</u>	845	<u>874</u>	882	931	999
N3		EF10	EF10	0.32	0.91	4	<u>174</u>	318	323	<u>346</u>	350	362
N4		EF10	EF10	0.70	0.91	4	<u>148</u>	278	295	315	<u>330</u>	340
N5		EF10	EF10	0.40	0.83	10	<u>214</u>	361	<u>364</u>	373	412	471
N6		EF10	EF10	0.69	0.88	10	<u>188</u>	348	<u>364</u>	366	376	405
C7		MS15	EF10	0.36	0.87	7	<u>203</u>	364	380	427	445	507
C8		MS15	EF10	0.69	0.87	7	<u>205</u>	463	492	554	<u>557</u>	590
M5		MS30	EF10	0.36	0.87	7	<u>203</u>	375	384	462	469	574
M6		MS30	EF10	0.69	0.87	7	<u>208</u>	499	518	627	630	<u>639</u>

decreases when the Young's modulus of the inclusion decreases. As a result, this optimization reveals that a change of Young's modulus tunes the starting mode around which the broadband vibration attenuation is activated. The specific origins of this mechanism of substantial vibration suppression are uncovered in Sec. 6.5.

Fig. 4(c) and (d) are the respectively the results of the TF reductions (objective function A) and TF reductions per mass (objective function B) for the six inclusions. For the inclusions S1, C3, and C5 having with small central cores and those



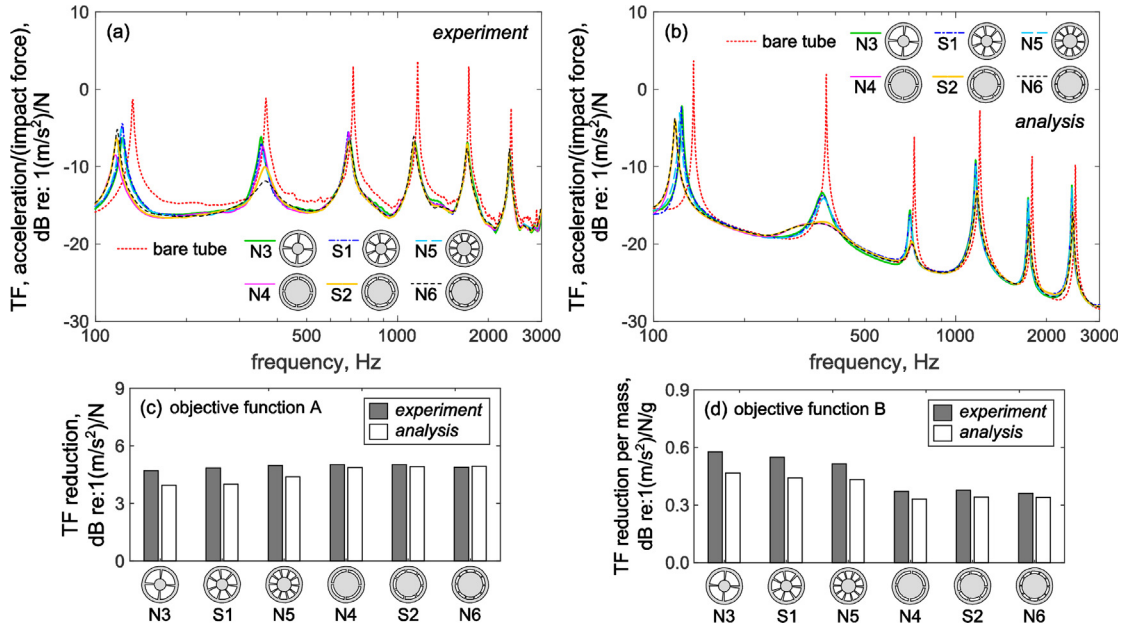
**Fig. 4.** Comparisons of six metamaterial inclusions, including S1, C3, C5, S2, C4 and C6, on (a) experimental TF frequency responses, (b) analytical TF frequency responses, (c) experimental and analytical TF reductions, and (d) experimental and analytical TF reductions per mass from 85 Hz to 3000 Hz.

inclusions S2, C4, and C6 having large cores, the TF reductions in Fig. 4(c) are seen to decrease when the Young's modulus increases. This trend is observed in experiments as well as through the analysis. For the objective function B for TF reductions per mass in Fig. 4(d), the results all together show that the inclusions composed with more compliant materials (grey EF10 inclusions) yield greater TF reductions for any given cross-section geometry. These trends agree with the finding that the starting mode of more substantial vibration attenuation decreases with decrease in the Young's modulus, thus resulting in greater TF reduction or overall TF reduction per mass at frequencies around and higher than the resonance near the starting mode.

## 6.2. Optimization by change of the number of radially arrayed beams

The results of Sec. 6.1 indicate that optimal single-material inclusions utilize the more compliant EF10 material and possess slender radially beams. The findings also illustrate that softer inclusion materials may reduce the frequency for the starting mode that yields greater overall TF reduction. The dynamic stiffness of the inclusion is therefore tailored by change in the Young's modulus and the cross-section geometry. It thus is logical to study the influence of optimizing inclusions where other characteristics of the radially arrayed beams are changed. Here, the number of radially arrayed beams is included as an optimization parameter. The optimizations carried out in this Sec. 6.2 consider the radius ratio, open angle ratio, and the inclusion material as the optimization parameters where the number of radially arrayed beams may be 4, 7, or 10. After undertaking the optimization with 4 radially arrayed beams, inclusions N3 and N4 are found to maximize objective functions B and A, respectively. Similarly, for 10 radially arrayed beams, inclusions N5 and N6 maximize objective functions B and A, respectively. The inclusions S1 and S2 are the counterpart optimized inclusions using 7 radially arrayed beams, as reported in Sec. 6.1. Qualitatively, the inclusions N3, S1, and N5 are made using the softest material EF10 and have small central cores and slender radial beams. Comparatively, the inclusions N4, S2, and N6 are fabricated using EF10 and have large cores with slender radial beams. The detailed parameters of the inclusions are given in Table 4.

Fig. 5(a) and (b) are respectively the experimental and analytical frequency responses of the host tube when pairs of the inclusions S1, S2, N3, N4, N5, and N6 are placed at the tube ends. In both the experimental Fig. 5(a) and analytical results Fig. 5(b), the starting mode for greater broadband attenuation of the host tube vibration is the second mode. This is observed for all six inclusions, which are all composed from the EF10 material yet have different numbers of radial beams. This suggests that the number of radially arrayed beams in the inclusion cross-section geometry has little influence to tailor the starting modes of broadband vibration attenuation, at least for the examples considered here. More so observed analytically in Fig. 5(b), the inclusions with smaller central cores, such as N3, S1, and N5, yield less attenuation of the host tube vibration than the inclusions with larger cores, such as N4, S2, and N6. Fig. 5(c) and (d) are the TF reductions (objective function A) and TF reductions per mass (objective function B) of the six inclusions, respectively. The experimental TF reductions of the six



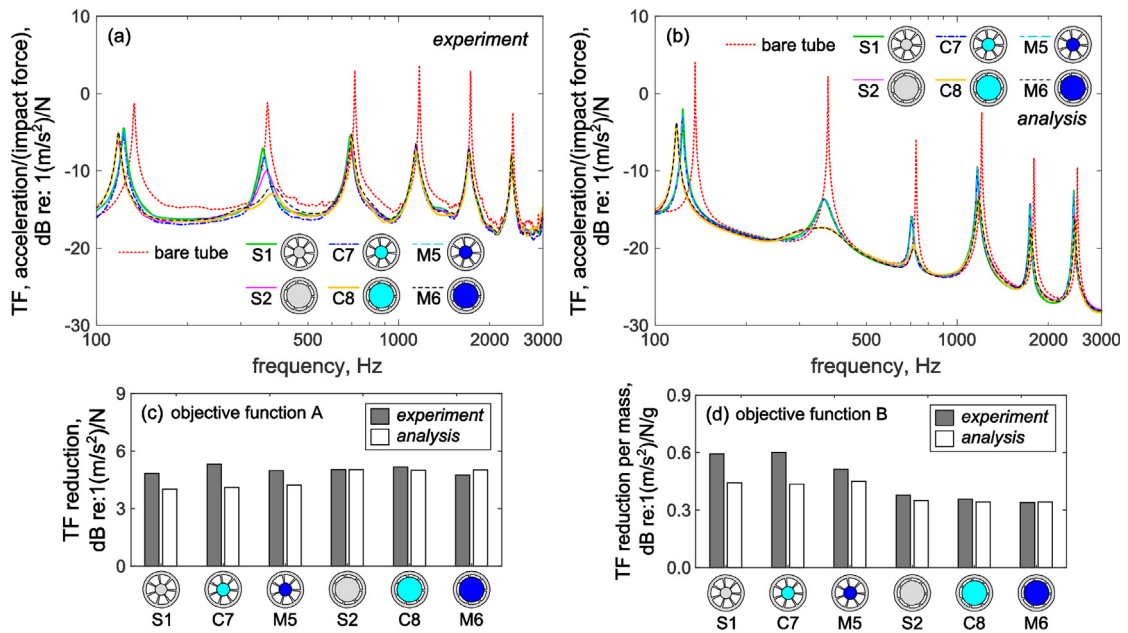
**Fig. 5.** Comparisons of six metamaterial inclusions, including N3, S1, N5, N4, S2 and N6, on (a) experimental TF frequency responses, (b) analytical TF frequency responses, (c) experimental and analytical TF reductions, and (d) experimental and analytical TF reductions per mass from 85 Hz to 3000 Hz.

inclusions are all approximately 5 dB. The analytical TF reductions of the inclusions with smaller cores (N3, S1, and N5) and the inclusions with larger cores (N2, S2, and N6) are approximately 4 dB and 5 dB, respectively. Given the conditions on which these inclusions are optimized, the results suggest that the number of slender radially array beams has little influence on the broadband vibration attenuation mechanisms. In addition, considering the analytical and experimental TF reductions per mass in Fig. 5(d), the inclusions with smaller central cores yield greater overall vibration attenuation per mass than the inclusions with larger cores.

### 6.3. Optimization of multi-material metamaterial inclusions

The results of the prior Secs. 6.1 and 6.2 give thorough evidence that the dynamic stiffness of the inclusion cross-section geometry is factor of inclusion behavior that is changed during the evolutionary optimization by the open angle ratio, radius ratio, and Young's modulus. Advancing this understanding, here the potential to design the inclusions with multiple materials is explored. The multi-material inclusions may utilize one material for the bulk/core layer, and another material for the porous and annular metamaterial layers. Since the number of radially arrayed beams in the porous metamaterial is seen to have little influence on tuning the broadband vibration attenuation ability, here all inclusions are optimized with 7 radial beams. The optimized multi-material inclusions obtained by GA with objective function B and A are inclusions M5 and M6, respectively. Inclusions M5 and M6 use the stiffer MS30 in the bulk/core metamaterial layer and use the softest EF10 in the porous and annular metamaterial. These inclusions M5 and M6 also have slender radial beams. The inclusions C7 and C8 have the same geometry as M5 and M6 but provide comparison to the optimized state by using the sub-optimal material MS15 in the bulk layers and use EF10 in the porous and annular metamaterial layers. The detailed parameters of the inclusions are given in Table 4.

Fig. 6(a) and (b) are respectively the experimental and analytical TF frequency responses of the host tube with pairs of inclusions S1, S2, M5, M6, C7, or C8 embedded at each end. For inclusions S1, C7, and M5, the narrowband TFs reveal negligible change resulting from change in the Young's modulus of the central bulk metamaterial layer. Comparatively for the inclusions with larger cores, such as S2, C8, and M6, the frequency responses are largely uninfluenced by change of the Young's modulus of the bulk metamaterial layer, excepting for the second mode in the experimental results Fig. 6(a). As shown in Fig. 6(b), the starting modes for greater broadband attenuation of the host tube vibration are uniformly found to be the second mode. This mode is also seen in the experimental evidence Fig. 6(a) to reveal a cut-on of more substantial vibration reduction. For the 6 inclusions considered here, the porous and annular metamaterial layers are composed from the softest material, EF10. This indicates that the Young's modulus of the bulk metamaterial layer has little influence to tailor the starting mode at which the broadband vibration attenuation is triggered. The overall TF reductions and TF reductions per mass are shown in Fig. 6(c) and (d). It is also seen considering such broadband metrics that the inclusions with smaller cores yield greater vibration attenuation per mass and that the Young's modulus of the bulk metamaterial layer has negligible influence to change the overall TF reduction. The results in Sec. 6.1 found that the single-material metamaterial inclusions fabricated from softer materials,



**Fig. 6.** Comparisons of six metamaterial inclusions, including S1, C7, M5, S2, C8 and M6, on (a) experimental TF frequency responses, (b) analytical TF frequency responses, (c) experimental and analytical TF reductions, and (d) experimental and analytical TF reductions per mass from 85 Hz to 3000 Hz.

namely the EF10 silicone rubber, result in greater broadband vibration attenuation. Together with the results of this Sec. 6.3, it is evident that the Young's modulus of the radially arrayed beams is specifically the more influential design parameter to govern the broadband vibration attenuation capability when coupled with optimal design of the slenderness of the radially arrayed beams.

#### 6.4. TMD and CLD effects in metamaterial inclusions

The optimization results of Secs. 6.1 to 6.3 reveal that the Young's modulus of porous and annular metamaterial layers is highly influential to tailor the dynamic stiffness of the inclusions and thus the vibration attenuation ability. To investigate how such broadband vibration attenuation is manifest based on the transition from TMD-like response to CLD-like behavior, the FE model results for the displacement amplitudes for inclusions C3, C4, C5, and C6 are shown in Fig. 7. The total displacement magnitudes for the inclusions C3, C4, C5, and C6 around the resonant frequencies for the forced cylindrical tube are respectively shown in Fig. 7(a), (b), (c), and (d). Inclusions C3 and C4 are made using MS15, while inclusions C5 and C6 are made using the stiffer MS30. In Fig. 4(a), the data report two narrowband reductions of the TF around 716 Hz and 687 Hz, which are around the third modes when inclusions C5 and C6 are utilized.

Similar to the displacement distributions around the first and second mode natural frequencies in Fig. 3(a,c) for EF10 inclusions (S1: 127 Hz and 370 Hz; S2: 119 Hz and 396 Hz), the MS15 inclusions (C3: 345 Hz and 711 Hz; C4: 345 Hz and 762 Hz) and the MS30 inclusions (C5: 345 Hz, 664 Hz, and 905 Hz; C6: 334 Hz, 641 Hz, and 1004 Hz) show respectively in Fig. 7(a,c) and (b,d) greater net deformation in the bulk layers than in the porous or annular layers around the second and third modes. Since the EF10 inclusions S1 and S2 exhibit the starting mode of broadband vibration attenuation closer to the second mode of the system, such as seen in Fig. 2(a and b), these results of Fig. 7 suggest that a similar vibration attenuation mechanism is induced for the inclusions composed from MS15 or MS30. The bulk metamaterial layers also vibrate vertically and laterally. Yet, this translational-and-shear TMD-like behavior is triggered around the third mode of the system using inclusions C3, C4, C5, or C6 according to the reduction of narrowband TFs in Fig. 4(a and b) at the frequencies around the third modes.

Furthermore, similar to the displacement distributions seen for the EF10 inclusions (S1: 711 Hz and 1152 Hz; S2: 711 Hz and 1152 Hz) around the third and fourth modes in Fig. 3(a,c), for the MS15 inclusions around the fourth and fifth modes (C3: 1192 Hz and 1741 Hz; C4: 1192 Hz and 1802 Hz) and for the MS30 inclusions around the fifth and sixth modes (C5: 1802 Hz and 2543 Hz; C6: 1802 Hz and 2543 Hz) the greater proportion of total deformation is concentrated in the porous and annular metamaterial layers in Fig. 7. This confirms that the vibration attenuation mechanisms that transition from TMD-like to CLD-like for the EF10-based metamaterial inclusions from the second to third modes appear for the MS15- and MS30-based metamaterial inclusions yet transition from the third to fourth modes. This indicates that the Young's modulus of the

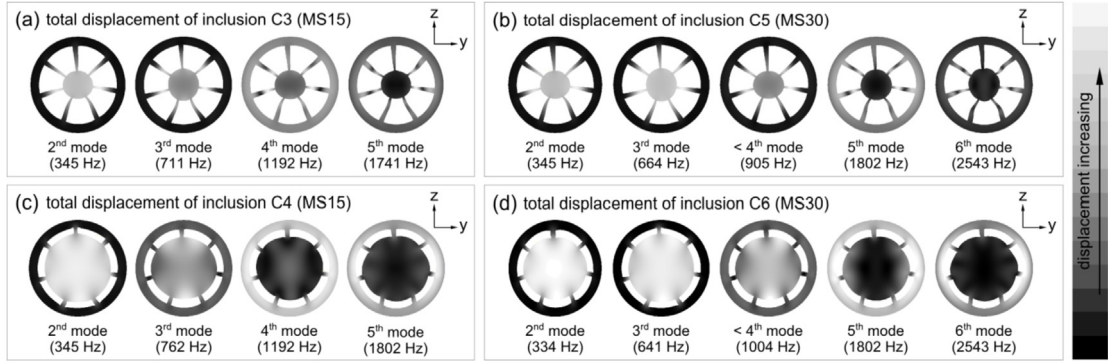


Fig. 7. Total displacement contours of (a) inclusion C3, (b) inclusion C5, (c) inclusion C4, and (d) inclusion C6. Inclusion C3 and inclusion C4 are made by MS15, and the contours are for the second, third, fourth and fifth modes. Inclusion C5 and C6 are made by MS30, and the contours are for the second, third, fifth and sixth modes.

cylindrical metamaterial inclusions is a key factor to determine the transition of dynamic behavior from TMD-like to CLD-like response.

### 6.5. Fundamental dynamics characteristics of the metamaterial inclusions

To more explicitly scrutinize the combined translational- and shear-based vibration attenuation mechanisms for the inclusions, the FE model geometry is modified to give attention only to the metamaterials. Specifically, the eigenfrequencies and eigenmodes of the metamaterial inclusions are determined when the outer circumferential surface of the cylindrical sections of the inclusion is held fixed. To eliminate the computation of modes that would not be greatly excited according to the lateral host tube motion studied here, no deformation in the  $y$  axis is permitted.

Fig. 8 presents the lowest six eigenmodes and normalized eigenfrequencies for two single-material metamaterial inclusions with radius ratio  $R^b/R^h = 0.32$  and open angle ratio  $\alpha/\beta = 0.85$  in Fig. 8(a), and with radius ratio  $R^b/R^h = 0.68$  and open angle ratio  $\alpha/\beta = 0.87$  in Fig. 8(b). The geometric parameters, materials, and lowest six eigenfrequencies of inclusions are given in Table 4. Through extensive assessment of the eigenfrequencies, there are consistent proportionalities uncovered by taking ratios of the eigenfrequencies among inclusion geometries and materials. It is found that the eigenfrequencies may be normalized according to the design parameters. The normalized eigenfrequency  $\bar{\omega}$  is

$$\bar{\omega} = \frac{2\pi f \sqrt{\rho^m R^h}}{\sqrt{E^m}} \tag{16}$$

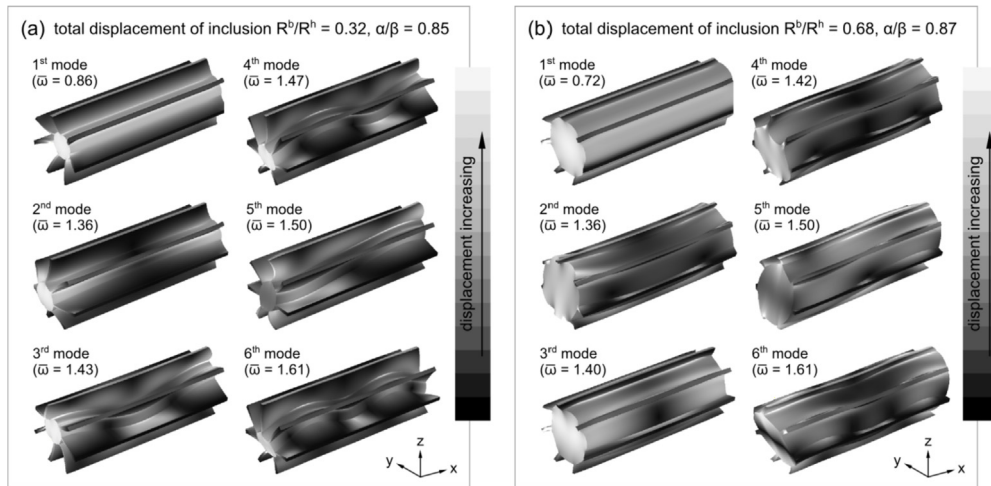


Fig. 8. Mode shapes for the lowest six modes of (a) inclusion with normalized radius  $R^b/R^h = 0.32$ , and open angle ratio  $\alpha/\beta = 0.85$ ; (b) inclusion with normalized radius  $R^b/R^h = 0.68$ , and open angle ratio  $\alpha/\beta = 0.87$ .

where  $f$ ,  $\rho^m$ , and  $E^m$  are respectively the eigenfrequency in Hz, density in  $\text{kg/m}^3$ , and Young's modulus in Pa of a single-material inclusion. The first and second modes in Fig. 8(a) and the first and third modes in Fig. 8(b) reveal pure shear deformation between the central bulk layer and outer annular layer (removed from the images for sake of visualization). Because the lateral force excitation would not excite such pure shear modes, they are not considered as mechanisms by which broadband vibration attenuation is achieved. The eigenfrequencies of pure shear modes are underlined in Table 4 to identify these special cases from the remainder of the mode shapes relevant for vibration suppression. The eigenmodes exhibiting both transverse and shear deformations are the third, fourth, fifth, and sixth modes in Fig. 8(a), and the second, fourth, fifth, and sixth modes in Fig. 8(b). Hence, the lowest excitable normalized eigenfrequencies for inclusions with  $R^b/R^h = 0.32$  and  $\alpha/\beta = 0.85$  is 1.43, and with  $R^b/R^h = 0.68$  and  $\alpha/\beta = 0.87$  is 1.36.

When the excitable eigenfrequency range of the inclusion is around the resonant frequencies of the cylindrical tube, the translational-and-shear modes in the metamaterials may be excited. These reactions assist to dissipate the cylindrical tube vibration through TMD-like absorption mechanisms at lower frequencies. In Table 4, for the EF10 inclusions S1 and S2, the lowest excitable eigenfrequencies are 363 Hz and 345 Hz, which are respectively 1.5% and 6.4% less than the second mode natural frequency of the cylindrical tube (368.5 Hz). Regarding the MS15 inclusions C3 and C4, the lowest excitable eigenfrequencies are 728 Hz and 690 Hz, which are respectively 1.6% and 3.7% less than the third mode eigenfrequency of the cylindrical tube (716.5 Hz). Finally, for the stiffer MS30 inclusions C5 and C6, the lowest excitable eigenfrequencies are 888 Hz and 845 Hz, which are also 23.9% and 22.0% less than the third mode eigenfrequency of the tube. Together, the results explain the origin of the frequency range wherein the metamaterial inclusions trigger exceptional broadband vibration damping. The lowest frequency eigenmodes of the EF10, MS15, and MS30 inclusions having both translational and shear deformations are triggered in a way that “cuts on” the vibration damping effects to the cylindrical tube. According to the discoveries of this work, the metamaterial inclusions can be designed for such exceptional vibration damping, with knowledge of the resonant frequencies of the host structure, using Eq. (16).

Unlike lightly-damped multi-dimensional vibration absorbers [29–31], the metamaterial inclusions studied here exhibit considerable damping (for instance, see Table 3), so that the frequency response of the cylindrical tube does not reveal an increasing number of resonant frequencies with the addition of the inclusions. The most similar manifestation of the traditional vibration absorber behavior induced in the TF for the tube occurs around the frequency where the lowest order translational and shear mode is excited, such as around 350 Hz in Fig. 2(a,b,c). Above this region, the metamaterial inclusions provide CLD-like vibration damping according to the short wavelengths of the modes induced in the inclusions compared to the structural dynamics. These findings underscore the duality of vibration absorption and vibration damping mechanisms enabled by the optimized metamaterial inclusions uncovered in this work.

For the inclusions N3, N4, N5, and N6 that possess 4, 4, 10, and 10 radially arrayed beams, the lowest excitable eigenfrequencies are respectively 318 Hz, 278 Hz, 361 Hz, and 348 Hz. These are also near to the second mode natural frequency of the tube. Regarding the multi-material inclusions C7, C8, M5, and M6, the lowest excitable eigenfrequencies are respectively 364 Hz, 463 Hz, 375 Hz, and 499 Hz. Likewise, these eigenfrequencies are also around the second mode natural frequency of the tube. These values and similarities suggest that the number of radially arrayed beams in the porous metamaterial layer and the Young's modulus of bulk metamaterial layer have less influence on changing the lowest excitable eigenfrequencies of inclusion for vibration attenuation of the host structure. Thus, the Young's modulus of the bulk metamaterial alone and the number of radially arrayed beams may not be critical factors in a tuning strategy for greater attenuation of the tube vibrations. These results support the findings in Sec. 6.2 and 6.3.

Within the specific context of attenuating the cylindrical tube vibrations, the analytical model results, finite element simulations, and experimental results of this work all conclude that the material selection of the porous and annular metamaterial layers is the most influential design parameter to tailor the broadband vibration suppression ability. Overall, the Young's modulus of annular and porous metamaterial layers largely govern the lowest excitable eigenfrequencies of metamaterial inclusions, while the number of radially arrayed beams and the Young's modulus of the bulk metamaterial layer are important but not critical determinants to the vibration suppression capability.

## 7. Conclusions

This research developed an analytical model and genetic algorithm optimization approach to study cylindrical metamaterial inclusions that maximize broadband attenuation of a hollow tube vibrations. The metamaterial inclusions have central cores, a layer of radially arrayed beams, and an annular layer at the inclusion periphery. Following verification by finite element simulation and validation through experiments, the optimized inclusions are scrutinized to uncover the working mechanisms of the ideal vibration suppression behavior. The mechanism of initiating broadband vibration suppression at lower frequencies is discovered to be associated with triggering the numerous low order eigenmodes of the metamaterial inclusions. The frequencies at which these eigenmodes occur are largely associated with the selection of the Young's modulus of the annular and porous metamaterial layers, and are weakly dependent on the number of radially arrayed beams and the Young's modulus of the core, bulk layer. Metamaterial inclusions with softer radially arrayed beams and annular layers exhibit the lowest excitable eigenfrequencies and thus lead to the greatest broadband vibration attenuation. A mathematical expression is revealed from the results to accelerate the design of the inclusions by selecting key design parameters so that the lowest eigenfrequencies of the inclusions coincide with the vibration frequencies to be attenuated. At higher frequencies

of host structure response, the damping observed in the frequency response results from the constrained layer damping-like actions of the inclusions on the host tube, since the wavelengths of metamaterial vibrations is much less than the host tube wavelength. These insights will greatly accelerate the design of metamaterial inclusions to attenuate practical tubular structures found in a wide variety of engineering applications.

## Acknowledgments

This work is supported by The Ohio State University Simulation Innovation and Modeling Center via Honda Research and Development Americas, Inc.

## Appendix

### A.1. Components of mass matrix

$$\mathbf{M} = \begin{bmatrix} M_{fp}^{hbhb} & M_{fq}^{hb1b} & M_{fr}^{hb1s} & M_{fs}^{hb1t} & \dots & M_{fq}^{hmbm} & M_{fr}^{hmbms} & M_{fs}^{hmbmt} \\ & M_{gq}^{1b1b} & M_{gr}^{1b1s} & M_{gs}^{1b1t} & 0 & 0 & 0 & 0 \\ & & M_{hr}^{1s1s} & M_{hs}^{1s1t} & \vdots & \vdots & \vdots & \vdots \\ & & & M_{is}^{1t1t} & 0 & \vdots & \vdots & \vdots \\ & & & & \ddots & 0 & 0 & 0 \\ & \text{sym} & & & & M_{gq}^{mbmb} & M_{gr}^{mbms} & M_{gs}^{mbmt} \\ & & & & & & M_{hr}^{msms} & M_{hs}^{msmt} \\ & & & & & & & M_{is}^{mtmt} \end{bmatrix} \quad (\text{A.1.1})$$

$$M_{fp}^{hbhb} = \frac{2\rho^h I^h}{L} \int_{-1}^1 \phi_p^{hb'} \phi_f^{hb'} d\xi + \frac{\rho^h A^h L}{2} \int_{-1}^1 \phi_p^{hb} \phi_f^{hb} d\xi + \frac{2(\rho^a I_{10}^a + \rho^p I_{10}^p)}{L^m} \int_{-1}^1 \phi_p^{hb'} \phi_f^{hb'} d\xi^m + \frac{(\rho^a A_{30}^a + \rho^p A_{30}^p) L^m}{2} \int_{-1}^1 \phi_p^{hb} \phi_f^{hb} d\xi^m \quad (\text{A.1.2})$$

$$M_{fq}^{hmbm} = \frac{(\rho^a A_{34}^a + \rho^p A_{34}^p) L^m}{4} \int_{-1}^1 \phi_f^{hb} \phi_q^{mb} d\xi^m \quad (\text{A.1.3})$$

$$M_{fr}^{hmbms} = \frac{\rho^a I_{15}^a + \rho^p I_{15}^p}{2} \int_{-1}^1 \phi_f^{hb'} \phi_r^{ms} d\xi^m \quad (\text{A.1.4})$$

$$M_{fs}^{hmbmt} = \frac{\rho^p I_{36}^p L^m}{4} \int_{-1}^1 \phi_f^{hb} \phi_s^{mt} d\xi^m \quad (\text{A.1.5})$$

$$M_{gq}^{mbmb} = \frac{(\rho^b A_{31}^b + \rho^a A_{31}^a + \rho^p A_{31}^p) L^m}{2} \int_{-1}^1 \phi_q^{mb} \phi_g^{mb} d\xi^m \quad (\text{A.1.6})$$

$$M_{gr}^{mbms} = 0 \quad (\text{A.1.7})$$

$$M_{gs}^{mbmt} = \frac{\rho^p I_{38}^p L^m}{4} \int_{-1}^1 \phi_g^{mb} \phi_s^{mt} d\xi^m \quad (\text{A.1.8})$$



$$M_{hr}^{msms} = \frac{(\rho^b I_{12}^b + \rho^a I_{12}^a + \rho^p I_{12}^p) L^m}{2} \int_{-1}^1 \phi_r^{ms} \phi_h^{ms} d\zeta^m \tag{A.1.9}$$

$$M_{hs}^{msmt} = 0 \tag{A.1.10}$$

$$M_{is}^{mtmt} = \frac{[\rho^b (I_{23}^b + I_{33}^b) + \rho^p (I_{23}^p + I_{33}^p)] L^m}{2} \int_{-1}^1 \phi_s^{mt} \phi_i^{mt} d\zeta^m \tag{A.1.11}$$

The constants of area and area moment inertia from Eq. (A.1.2) to Eq. (A.1.11) are listed in Ref. [20].

A.2 Components of stiffness matrix

$$K = \begin{bmatrix} K_{fp}^{hhbb} & K_{fq}^{hb1b} & K_{fr}^{hb1s} & K_{fs}^{hb1t} & \dots & K_{fq}^{hmbb} & K_{fr}^{hmbms} & K_{fs}^{hmbmt} \\ & K_{gq}^{1b1b} & K_{gr}^{1b1s} & K_{gs}^{1b1t} & 0 & 0 & 0 & 0 \\ & & K_{hr}^{1s1s} & K_{hs}^{1s1t} & \vdots & \vdots & \vdots & \vdots \\ & & & K_{is}^{1t1t} & 0 & \vdots & \vdots & \vdots \\ & & & & \ddots & 0 & 0 & 0 \\ & & & & & K_{gq}^{mbmb} & K_{gr}^{mbms} & K_{gs}^{mbmt} \\ & \text{sym} & & & & & K_{hr}^{msms} & K_{hs}^{msmt} \\ & & & & & & & K_{is}^{mtmt} \end{bmatrix} \tag{A.2.1}$$

$$K_{fp}^{hhbb} = \frac{8\tilde{E}^h I^h}{L^3} \int_{-1}^1 \phi_p^{hb''} \phi_f^{hb''} d\zeta + \frac{8(\tilde{E}^a I_{10}^a + \tilde{E}^p I_{10}^p)}{(L^m)^3} \int_{-1}^1 \phi_p^{hb''} \phi_f^{hb''} d\zeta^m + \frac{2[\tilde{G}^a k^a (A_{50}^a + A_{60}^a) + \tilde{G}^p k^p (A_{50}^p + A_{60}^p)]}{L^m} \int_{-1}^1 \phi_p^{hb'} \phi_f^{hb'} d\zeta^m \tag{A.2.2}$$

$$+ \frac{(\tilde{E}^a I_{30}^a + \tilde{E}^p I_{30}^p) L^m + (\tilde{G}^a k^a J_{40}^a + \tilde{G}^p k^p J_{40}^p) L^m}{2} \int_{-1}^1 \phi_p^{hb} \phi_f^{hb} d\zeta^m$$

$$K_{fq}^{hmbb} = -\frac{\tilde{G}^a k^a A_{54}^a + \tilde{G}^p k^p A_{54}^p}{L^m} \int_{-1}^1 \phi_f^{hb'} \phi_q^{mb'} d\zeta^m - \frac{(\tilde{E}^a I_{34}^a + \tilde{E}^p I_{34}^p) L^m + (\tilde{G}^a k^a J_{44}^a + \tilde{G}^p k^p J_{44}^p) L^m}{4} \int_{-1}^1 \phi_q^{mb} \phi_f^{hb} d\zeta^m \tag{A.2.3}$$

$$K_{fr}^{hmbms} = \frac{2(\tilde{E}^a I_{15}^a + \tilde{E}^p I_{15}^p)}{(L^m)^2} \int_{-1}^1 \phi_f^{hb''} \phi_r^{ms'} d\zeta^m - \frac{\tilde{G}^a k^a (A_{55}^a + A_{65}^a) + \tilde{G}^p k^p (A_{55}^p + A_{65}^p)}{2} \int_{-1}^1 \phi_f^{hb'} \phi_r^{ms} d\zeta^m \tag{A.2.4}$$

$$K_{fs}^{hgmt} = -\frac{\tilde{G}^p k^p (J_{56}^p - J_{66}^p)}{L^m} \int_{-1}^1 \phi_f^{hb'} \phi_s^{mt'} d\xi^m - \frac{(\tilde{E}^p J_{36}^p - \tilde{G}^p k^p J_{46}^p) L^m}{4} \int_{-1}^1 \phi_f^{hb} \phi_s^{mt} d\xi^m \tag{A.2.5}$$

$$K_{gq}^{mbmb} = \frac{2(\tilde{G}^b k^b A_{51}^b + \tilde{G}^a k^a A_{51}^a + \tilde{G}^p k^p A_{51}^p)}{L^m} \int_{-1}^1 \phi_q^{mb'} \phi_g^{mb'} d\xi^m + \frac{(\tilde{E}^a I_{31}^a + \tilde{E}^p J_{31}^p) L^m + (\tilde{G}^a k^a J_{41}^a + \tilde{G}^p k^p J_{41}^p) L^m}{2} \int_{-1}^1 \phi_q^{mb} \phi_g^{mb} d\xi^m \tag{A.2.6}$$

$$K_{gr}^{mbms} = -\frac{\tilde{G}^b k^b A_{57}^b - \tilde{G}^a k^a A_{57}^a - \tilde{G}^p k^p A_{57}^p}{2} \int_{-1}^1 \phi_g^{mb'} \phi_r^{ms} d\xi^m \tag{A.2.7}$$

$$K_{gs}^{mbmt} = \frac{\tilde{G}^p k^p J_{58}^p}{L^m} \int_{-1}^1 \phi_g^{mb'} \phi_s^{mt'} d\xi^m + \frac{(\tilde{E}^p J_{38}^p - \tilde{G}^p k^p J_{48}^p) L^m}{4} \int_{-1}^1 \phi_g^{mb} \phi_s^{mt} d\xi^m \tag{A.2.8}$$

$$K_{hr}^{msms} = \frac{2(\tilde{E}^b I_{12}^b + \tilde{E}^a I_{12}^a + \tilde{E}^p I_{12}^p)}{L^m} \int_{-1}^1 \phi_r^{ms'} \phi_h^{ms'} d\xi^m + \frac{[\tilde{G}^b k^b A_{52}^b + \tilde{G}^a k^a (A_{52}^a + A_{62}^a) + \tilde{G}^p k^p (A_{52}^p + A_{62}^p)] L^m}{2} \int_{-1}^1 \phi_r^{ms} \phi_h^{ms} d\xi^m \tag{A.2.9}$$

$$K_{hs}^{msmt} = -\frac{\tilde{G}^p k^p (J_{69}^p - J_{59}^p)}{2} \int_{-1}^1 \phi_h^{ms} \phi_s^{mt'} d\xi^m \tag{A.2.10}$$

$$K_{is}^{mtmt} = \frac{2[\tilde{G}^b k^b (J_{53}^b + J_{63}^b) + \tilde{G}^p k^p (J_{53}^p + J_{63}^p)]}{L^m} \int_{-1}^1 \phi_s^{mt'} \phi_i^{mt'} d\xi^m + \frac{[\tilde{E}^p (A_{23}^p + A_{33}^p) + \tilde{G}^p k^p A_{43}^p] L^m}{2} \int_{-1}^1 \phi_s^{mt} \phi_i^{mt} d\xi^m \tag{A.2.11}$$

The constants of area and area moment inertia from Eq. (A.2.2) to Eq. (A.2.11) are listed in Ref. [20].

### A.3 Components of Kelvin-Voigt damping matrix

$$C^{KV} = \begin{bmatrix} C_{fp}^{hbhb} & C_{fq}^{hb1b} & C_{fr}^{hb1s} & C_{fs}^{hb1t} & \dots & C_{fq}^{hbmb} & C_{fr}^{hbms} & C_{fs}^{hgmt} \\ & C_{gq}^{1b1b} & C_{gr}^{1b1s} & C_{gs}^{1b1t} & 0 & 0 & 0 & 0 \\ & & C_{hr}^{1s1s} & C_{hs}^{1s1t} & \vdots & \vdots & \vdots & \vdots \\ & & & C_{is}^{1t1t} & 0 & \vdots & \vdots & \vdots \\ & & & \ddots & \ddots & 0 & 0 & 0 \\ & \text{sym} & & & & C_{gq}^{mbmb} & C_{gr}^{mbms} & C_{gs}^{mbmt} \\ & & & & & & C_{hr}^{msms} & C_{hs}^{msmt} \\ & & & & & & & C_{is}^{mtmt} \end{bmatrix} \tag{A.3.1}$$

$$C_{fp}^{hbhb} = \frac{[C^a(I_{30}^a + J_{40}^a) + C^p(I_{30}^p + J_{40}^p)]L^m}{2} \int_{-1}^1 \phi_p^{hb} \phi_f^{hb} d\xi^m$$

$$+ \frac{2[C^a(A_{50}^a + A_{60}^a) + C^p(A_{50}^p + A_{60}^p)]}{L^m} \int_{-1}^1 \phi_p^{hb'} \phi_f^{hb'} d\xi^m + \frac{8(C^a I_{10}^a + C^p I_{10}^p)}{(L^m)^3} \int_{-1}^1 \phi_p^{hb''} \phi_f^{hb''} d\xi^m \quad (\text{A.3.2})$$

$$C_{fq}^{hmbm} = -\frac{C^a A_{54}^a + C^p A_{54}^p}{L^m} \int_{-1}^1 \phi_f^{hb'} \phi_q^{mb'} d\xi^m - \frac{[C^a(I_{34}^a + J_{44}^a) + C^p(I_{34}^p + J_{44}^p)]L^m}{4} \int_{-1}^1 \phi_f^{hb} \phi_q^{mb} d\xi^m \quad (\text{A.3.3})$$

$$C_{fr}^{hbms} = \frac{2(C^a I_{15}^a + C^p I_{15}^p)}{(L^m)^2} \int_{-1}^1 \phi_f^{hb''} \phi_r^{ms'} d\xi^m - \frac{C^a(A_{55}^a + A_{65}^a) + C^p(A_{55}^p + A_{65}^p)}{2} \int_{-1}^1 \phi_f^{hb'} \phi_r^{ms} d\xi^m \quad (\text{A.3.4})$$

$$C_{fs}^{hbmt} = -\frac{C^p(J_{56}^p - J_{66}^p)}{L^m} \int_{-1}^1 \phi_f^{hb'} \phi_s^{mt'} d\xi^m - \frac{C^p(J_{36}^p - J_{46}^p)L^m}{4} \int_{-1}^1 \phi_f^{hb} \phi_s^{mt} d\xi^m \quad (\text{A.3.5})$$

$$C_{gq}^{mbmb} = \frac{2(C^b A_{51}^b + C^a A_{51}^a + C^p A_{51}^p)}{L^m} \int_{-1}^1 \phi_q^{mb'} \phi_g^{mb'} d\xi^m$$

$$+ \frac{[C^a(I_{31}^a + J_{41}^a) + C^p(I_{31}^p + J_{41}^p)]L^m}{2} \int_{-1}^1 \phi_q^{mb} \phi_g^{mb} d\xi^m \quad (\text{A.3.6})$$

$$C_{gr}^{mbms} = -\frac{C^b A_{57}^b - C^a A_{57}^a - C^p A_{57}^p}{2} \int_{-1}^1 \phi_g^{mb'} \phi_r^{ms} d\xi^m \quad (\text{A.3.7})$$

$$C_{gs}^{mbmt} = \frac{C^p J_{58}^p}{L^m} \int_{-1}^1 \phi_g^{mb'} \phi_s^{mt'} d\xi^m + \frac{C^p(J_{38}^p - J_{48}^p)L^m}{4} \int_{-1}^1 \phi_g^{mb} \phi_s^{mt} d\xi^m \quad (\text{A.3.8})$$

$$C_{hr}^{msms} = \frac{2(C^b I_{12}^b + C^a I_{12}^a + C^p I_{12}^p)}{L^m} \int_{-1}^1 \phi_r^{ms'} \phi_h^{ms'} d\xi^m$$

$$+ \frac{[C^b A_{52}^b + C^a(A_{52}^a + A_{62}^a) + C^p(A_{52}^p + A_{62}^p)]L^m}{2} \int_{-1}^1 \phi_r^{ms} \phi_h^{ms} d\xi^m \quad (\text{A.3.9})$$

$$C_{hs}^{msmt} = -\frac{C^p(J_{69}^p - J_{59}^p)}{2} \int_{-1}^1 \phi_h^{ms} \phi_s^{mt'} d\xi^m \quad (\text{A.3.10})$$

$$C_{is}^{mtmt} = \frac{2[C^b(J_{53}^b + J_{63}^b) + C^p(J_{53}^p + J_{63}^p)]}{L^m} \int_{-1}^1 \phi_s^{mt'} \phi_i^{mt'} d\xi^m$$

$$+ \frac{C^p(A_{23}^p + A_{33}^p + A_{43}^p)L^m}{2} \int_{-1}^1 \phi_s^{mt} \phi_i^{mt} d\xi^m \quad (\text{A.3.11})$$

The constants of area and area moment inertia from Eq. (A.3.2) to Eq. (A.3.11) are listed in Ref. [20].

## References

- [1] M.R. Haberman, M.D. Guild, Acoustic metamaterials, *Phys. Today* 69 (2016) 42–48.
- [2] K.H. Matlack, M. Serra-Garcia, A. Palermo, S.D. Huber, C. Daraio, Designing perturbative metamaterials from discrete models, *Nat. Mater.* 17 (4) (2018) 323.
- [3] H. Peng, P.F. Pai, H. Deng, Acoustic multi-stopband metamaterial plates design for broadband elastic wave absorption and vibration suppression, *Int. J. Mech. Sci.* 103 (2015) 104–114.
- [4] X. An, H. Fan, C. Zhang, Wave dispersion in one-dimensional periodic graded metacomposites, *J. Sound Vib.* 409 (2017) 217–226.
- [5] B. Essink, D. Inman, A comparison of damping and vibration absorption in metastructures, in: *Proceedings of the ISMA2016*, 2016, pp. 2025–2030. Leuven, Belgium.
- [6] Y. Chen, T. Li, F. Scarpa, L. Wang, Lattice metamaterials with mechanically tunable Poisson's ratio for vibration control, *Phys. Rev. Appl.* 7 (2017), 024012.
- [7] E. Baravelli, M. Ruzzene, Internally resonating lattices for bandgap generation and low-frequency vibration control, *J. Sound Vib.* 332 (2013) 6562–6579.
- [8] X.N. Liu, G.K. Hu, C.T. Sun, G.L. Huang, Wave propagation characterization and design of two-dimensional elastic chiral metacomposite, *J. Sound Vib.* 330 (2011) 2536–2553.
- [9] R. Zhu, X.N. Liu, G.K. Hu, C.T. Sun, G.L. Huang, A chiral elastic metamaterial beam for broadband vibration suppression, *J. Sound Vib.* 333 (2014) 2759–2773.
- [10] O. Abdeljaber, O. Avci, D.J. Inman, Optimization of chiral lattice based metastructures for broadband vibration suppression using genetic algorithms, *J. Sound Vib.* 369 (2016) 50–62.
- [11] M. Ranjbar, L. Boldrin, F. Scarpa, S. Neild, S. Patsias, Vibroacoustic optimization of anti-tetrachiral and auxetic hexagonal sandwich panels with gradient geometry, *Smart Mater. Struct.* 25 (5) (2016), 054012.
- [12] H.W. Dong, S.D. Zhao, Y.S. Wang, C. Zhang, Topology optimization of anisotropic broadband double-negative elastic metamaterials, *J. Mech. Phys. Solids* 105 (2017) 54–80.
- [13] X. Yang, Y.Y. Kim, Topology optimization for the design of perfect mode-converting anisotropic elastic metamaterials, *Compos. Struct.* 201 (2018) 161–177.
- [14] X.W. Yang, J.S. Lee, Y.Y. Kim, Effective mass density based topology optimization of locally resonant acoustic metamaterials for bandgap maximization, *J. Sound Vib.* 383 (2016) 89–107.
- [15] K.T. Tan, H.H. Huang, C.T. Sun, Optimizing the band gap of effective mass negativity in acoustic metamaterials, *Appl. Phys. Lett.* 101 (24) (2012) 241902.
- [16] Q. Chen, X. Zhang, B. Zhu, Design of buckling-induced mechanical metamaterials for energy absorption using topology optimization, *Struct. Multi-discip. Optim.* 58 (4) (2018) 1395–1410.
- [17] L. Zuo, S.A. Nayfeh, Minimax optimization of multi-degree-of-freedom tuned-mass dampers, *J. Sound Vib.* 272 (3–5) (2004) 893–908.
- [18] K.K. Reichl, D.J. Inman, Lumped mass model of a 1D metastructure for vibration suppression with no additional mass, *J. Sound Vib.* 403 (2017) 75–89.
- [19] J. Bishop, Q. Dai, Y. Song, R.L. Harne, Resilience to impact by extreme energy absorption in lightweight material inclusions constrained near a critical point, *Adv. Eng. Mater.* 18 (2016) 1871–1876.
- [20] S.L. Yeh, R.L. Harne, Tailoring concurrent shear and translational vibration control mechanisms in elastomeric metamaterials for cylindrical structures, *Mech. Syst. Signal Process.* 117 (2019) 609–633.
- [21] O. Beslin, J. Nicolas, A hierarchical functions set for predicting very high order plate bending modes with any boundary conditions, *J. Sound Vib.* 202 (5) (1997) 633–655.
- [22] G.R. Cowper, The shear coefficient in Timoshenko's beam theory, *J. Appl. Mech.* 33 (2) (1966) 335–340.
- [23] T. Kocatürk, M. Şimşek, Dynamic analysis of eccentrically prestressed viscoelastic Timoshenko beams under a moving harmonic load, *Comput. Struct.* 84 (31–32) (2006) 2113–2127.
- [24] T.C. Tsai, J.H. Tsau, C.S. Chen, Vibration analysis of a beam with partially distributed internal viscous damping, *Int. J. Mech. Sci.* 51 (11–12) (2009) 907–914.
- [25] W.R. Chen, Bending vibration of axially loaded Timoshenko beams with locally distributed Kelvin-Voigt damping, *J. Sound Vib.* 330 (13) (2011) 3040–3056.
- [26] W.R. Chen, Parametric studies on bending vibration of axially-loaded twisted Timoshenko beams with locally distributed Kelvin-Voigt damping, *Int. J. Mech. Sci.* 88 (2014) 61–70.
- [27] L. Dozio, On the use of the trigonometric Ritz method for general vibration analysis of rectangular Kirchhoff plates, *Thin-Walled Struct.* 49 (2011) 129–144.
- [28] A.M. Kabe, B.H. Sako, Issues with proportional damping, *AIAA J.* 54 (2016) 2864–2868.
- [29] M.S. Khun, H.P. Lee, S.P. Lim, Structural intensity in plates with multiple discrete and distributed spring-dashpot systems, *J. Sound Vib.* 276 (2004) 627–648.
- [30] D.J. Thompson, A continuous damped vibration absorber to reduce broad-band wave propagation in beams, *J. Sound Vib.* 311 (2008) 824–842.
- [31] J.C. Snowdon, Platelike dynamic vibration absorbers, *Trans. Am. Soc. Mech. Eng., J. Eng. Ind.* 97 (1975) 88–93.